Supporting Information

From Generation to Collection – Impact of Deposition Temperature on Charge Carrier Dynamics of High Performance Evaporated Organic Solar Cells

Richard Adam Pacalaj*, Yifan Dong, Ivan Ramirez, Roderick C.I. MacKenzie, Seyed Mehrdad Hosseini, Eva Bittrich, Julian Eliah Heger, Pascal Kaienburg, Subhrangsu Mukherjee, Jiaying Wu, Moritz Riede, Harald Ade, Peter Müller-Buschbaum, Martin Pfeiffer* and James Robert Durrant*

Methods

Device Preparation: All the layers of the vapour-processed solar cells were thermally evaporated in an ultra-high vacuum chamber onto the patterned ITO substrates. The electron transport layer consisted of a combination of n-doped and intrinsic C_{60} (5 nm and 15 nm, respectively). The active layer was subsequently deposited with the substrate either kept at room temperature or heated to 50 °C. Finally, a layer of 10 nm undoped BPAPF (Lumtec, Taiwan) and 20 nm p-doped BPAPF were deposited before finishing the device with 100 nm of Al. The active layer area was approximately 7.1 mm^2. The devices were encapsulated using a glass slide in nitrogen.

JV-Characterisation: *JV*-curves were collected using a Keithley 2400 voltage source. The light source is a Newport 92193A-1000 (AM1.5 G 100mW cm^{-2}) Xenon lamp calibrated by a silicon diode. The devices prepared by Heliatek GmbH were encapsulated while solution processed reference devices were kept in a nitrogen filled measurement chamber for all optoelectronic characterisations. External quantum efficiency measurements were carried out using a Quantum Design PV300 system.

Grazing-Incidence Wide-Angle X-Ray Scattering: The 2D GIWAXS data was measured with a laboratory-based instrument (Ganesha, SAXSLAB, Xenocs, Grenoble, France) with a photon wavelength of 1.54 Å and an incident angle set to 0.2°. A Pilatus 300k detector having a pixel size of 172 μm^2 was set at a 956 mm distance to the sample to detect and resolve the desired *q*-range. 1D radial cuts along *q* were obtained by azimuthal integration within the opening angle of 40° to the substrate normal. Peak center values were obtained by fitting Gaussian functions to the 1D radial cuts, and the respective lattice spacing d was calculated as:

$$d_{hkl} = \frac{2\pi}{q_{hkl}}$$

1D azimuthal cuts along χ were obtained by radial integration of the q_{100} and q_{010} reflexes, respectively, and multiplied with the Lorentz factor $sin^{[20]}(\chi)$ to visualize the material quantity of crystallites having a particular orientation to the substrate, edge-on, and face-on.

Resonant Soft X-Ray Scattering: The stack is SiN/C60 (10 nm)/BHJ (50 nm, D:A 3:2 wt%)/BPAPF(10 nm). The *40C* sample was 30 nm and its intensity scaled accordingly. Samples of the BHJ films were prepared for R-SoXS through evaporation on a 100 nm Si3N4 window (Silson, UK), whose temperature was controlled during position, for R-SoXS measurements. The 2-D R-SoXS data were collected at beamline BL 11.0.1.2[1] at the Advanced Light Source using a Peltier-cooled (-45 °C) in-vacuum [base pressure $\sim 10^{-9}$ kPa (10^{-8} mBar)] CCD detector (PI-MTE, Princeton Instruments, Trenton, New Jersey; 2048 × 2048 pixels). 1-D scattering profiles were obtained from the 2-D scattering patterns using a custom Nika analysis package (https://github.com/EliotGann/Eliots-NIKA)[2] and subsequently normalized for the instantaneous X-ray flux. The scattering intensity is affected by the distance traveled by the X-ray beam through the sample. R-SoXS scattering intensities were therefore normalized for absorption and film thickness.[3] *Further details of the analysis will be discussed below.*

Absorption Spectroscopy: UV-vis measurements were done on active layer films on glass using a UV-1601 Shimadzu spectrometer.

Photoluminescence Spectroscopy: PL spectra were collected using a home-built system consisting of a spectrograph (Kymera 193i, Andor) and a CCD camera (DU420A-BEX2-DD, Andor). A CW 532 nm laser diode module (THORLABS, CPS532[b]) was used for photoexcitation.

Transient Absorption Spectroscopy: A commercially available broadband pump-probe femtosecond (fs) transient absorption (TA) spectrometer Helios (Spectra Physics, Newport Corp.) was used to measure the TA spectra and kinetics for thin film samples. Ultrafast laser pulses (800 nm, 100 fs duration) were generated by a 1 kHz Ti:sapphire regenerative amplifier (Solstice, Spectra Physics, Newport Corp.). One portion of the 800 nm pulse was directed to an optical parametric amplifier (TOPAS Prime, Spectra-Physics) and a frequency mixer (Niruvis, Light Conversion) to tune the visible pump pulses at various wavelengths. The pump pulses

were modulated at a frequency of 500 Hz by a mechanical chopper. The rest of the 800 nm pulse was routed onto a mechanical delay stage with a 6 ns time window and directed through a non-linear crystal (sapphire for the visible region and YAG for the NIR region) to generate a white light probe ranging from 400 – 1600 nm. The probe pulse was split into two by a neutral density filter. One portion of the probe pulse served as the reference and was directly sent to the fiber-optic coupled multichannel spectrometers (CCD and InGaAs sensors). The rest of the probe pulse together with the pump pulse were focused onto the same spot on the samples with a beam size of around 0.5 mm2 before sending it to the spectrometer. To compensate the fluctuations, the measured spectrum was normalized to the reference spectrum and averaged for several scans to achieve a good signal-to-noise ratio. Data analysis was performed with the commercialized Surface Xplorer software unless otherwise stated.

Charge Extraction: Charge extraction measurements are carried out by illuminating the device while kept under open circuit conditions and simultaneously switching the illumination off and the device to short circuit and recording the resulting current transient using a Tektronix TDS3032B oscilloscope (1 MΩ input impedance, measured voltage drop across 50 Ω resistor and converted to a current measurement using Ohm's law). To obtain the total charge extracted from the device, the current transient is integrated. This is carried out for multiple illumination levels as previously described.[4] The total charge is corrected by determining the geometric capacitance from charge extraction measurements in the dark at reverse bias and subtracting the product of geometric capacitance and V_{OC} from the total charge. The switching is realised by MOSFETs controlled by the DAQCard to switch between open circuit and short circuit conditions and simultaneously breaking the circuit of the light source with a second MOSFET. The light source consists of a ring of 6 warm and 6 cold white light LEDs. Calibration of the LEDs is achieved by matching the J_{SC} to the measurement obtained from the solar simulator. The charge carrier density obtained from charge extraction at open circuit can be used together with transient photovoltage lifetime data (discussed below) collected under equivalent illumination conditions to calculate the bimolecular recombination coefficient. When keeping the device under short circuit conditions prior to switching the illumination off, the steady state charge carrier density at short circuit for varying light intensities can be measured. Following the analytical model by Shuttle *et al.* this can be used to calculate the effective mobility of the active layer.[5]

Transient Photovoltage: A Continuum Minilite II pulsed laser is used to generate a small perturbation voltage (532 nm, 5 ns) while the device is kept under open circuit conditions (1 MΩ input impedance of the oscilloscope) and illuminated by a ring of 6 warm and 6 cold white light LEDs. The decay of the small perturbation voltage back to the steady state V_{OC} is monitored by the oscilloscope. Fitting a single exponential yields the small perturbation lifetime from which the full charge carrier lifetime can be calculated as detailed by Shuttle *et al.* by multiplication with the experimentally determined recombination order.[6] Correcting the lifetime for capacitive effects as outlined by Credgington *et al.*[7] yields little change as the chemical capacitance outweighs the geometric capacitance in the region of interest (above 10 % sun intensity).

Transient Photocurrent and Differential Capacitance: Transient photocurrent measurements are carried out using the same pulsed laser condition as described above while the device is kept at short circuit in the dark. The current transient is recorded as described for the charge extraction measurements. The integrated current transient yields the charge generated by the laser pulse and can be used to calculate the differential capacitance as outline by Shuttle *et al.* when combined with the maximum voltage perturbation measured in the transient photovoltage measurements.[6] The geometric capacitance is determined by fitting the total differential capacitance with an exponential offset by a constant geometric capacitance term. The geometric capacitance is then subtracted from the total capacitance before the charge carrier density is calculated from the differential capacitance as outlined by Shuttle *et al.*[6] High resolution photocurrent transients for the determination of the energetic disorder of the active layer are carried out by recording the voltage drop across various resistances in the range of 50 Ω to 5000 Ω using the 1 MΩ input impedance of the oscilloscope. The different resistors enable us to increase the resolution of the resulting voltage measurements that are converted to current transients using Ohm's law. The transients are then stitched together by removing the early part dominated by the *RC*-time constant. The method has been previously outlined by Street.[8]
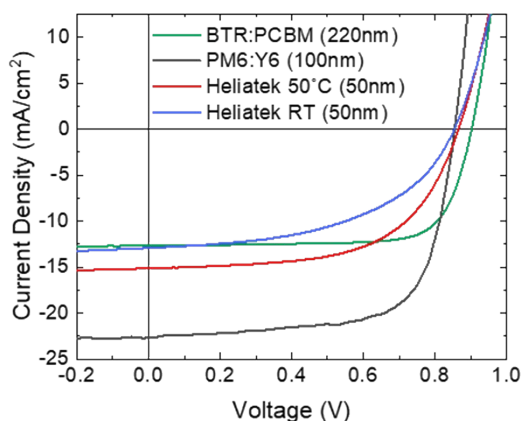
Drift-Diffusion Simulation: Please find detailed documentation about the software package OghmaNano under *https://www.oghma-nano.com/contact.html*.
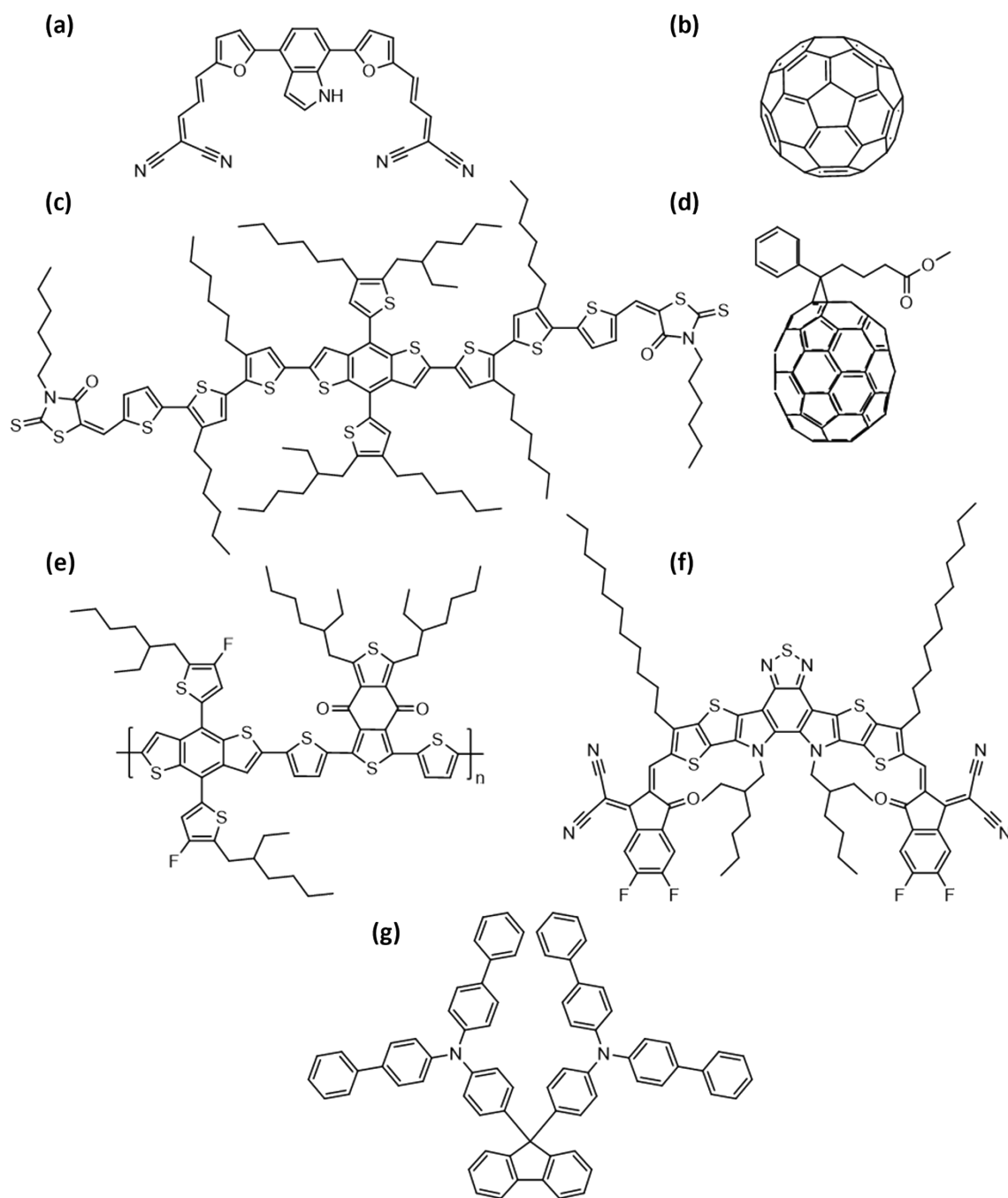
SI Figure 1. Chemical structure of active layer components and the organic hole transporting material BPAPF used in this paper: **(a)** DCV-V-Fu-Ind-Fu-V (2,2'-((2E,2'E)-((1H-indole-4,7-diyl)bis(furan-5,2-diyl))bis(prop-2-en-3-yl-1-ylidene))dimalononitrile) **(b)** C_{60} – fullerene **(c)** BTR (5,5'-[[4,8-bis[5-(2-ethylhexyl)-4-hexyl-2-thienyl]benzo[1,2-b:4,5-b']dithiophene-2,6-diyl]bis [(3',3"-dihexyl[2,2':5',2"-terthiophene]-5",5-diyl)methylidyne]] bis[3-hexyl-2-thioxo-4-thiazolidinone]) **(d)** $PC_{70}BM$ ([6,6]-Phenyl-C71-butyric acid methyl ester) **(e)** PM6 (Poly[(2,6-(4,8-bis(5-(2-ethylhexyl-3-fluoro)thiophen-2-yl)-benzo[1,2-b:4,5-b']dithiophene))-alt-(5,5-(1',3'-di-2-thienyl-5',7'-bis(2-ethylhexyl)benzo[1',2'-c:4',5'-c']dithiophene-4,8-dione)]) **(f)** Y6 (2,2'-((2Z,2'Z)-((12,13-bis(2-ethylhexyl)-3,9-diundecyl-12,13-dihydro-[1,2,5]thiadiazolo[3,4-e]thieno[2",3"':4',5']thieno[2',3':4,5]pyrrolo[3,2-g]thieno [2',3':4,5] thieno[3,2-b]indole-2,10-diyl)bis(methanylylidene))bis(5,6-difluoro-3-oxo-2,3-dihydro-1H-indene-2,1-diylidene))dimalononitrile) **(g)** BPAPF (9,9-Bis[4-(N,N-bis-biphenyl-4-yl-amino) phenyl]-9H-fluorene)

5
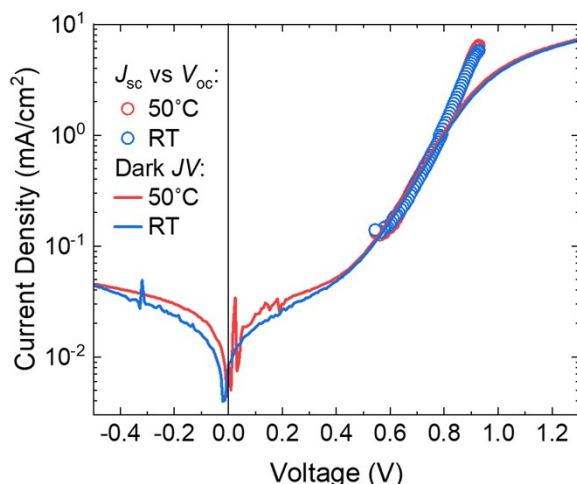
**SI Figure 2.** Dark JV-curves and J_{SC} versus V_{OC} of the RT and $50\,^{\circ}C$ devices.

|	J_{SC}	FF	V_{OC}	PCE
	[mA/cm^2]	[%]	[V]	[%]
DCV-V-Fu-Ind-Fu-V:C$_{60}$	12.9	50.5	0.850	5.54
(RT)	± 0.1	± 0.1	± 0.001	± 0.02
DCV-V-Fu-Ind-Fu-V:C$_{60}$	15.2	59.4	0.859	7.78
(50C)	± 0.1	± 0.1	± 0.001	± 0.02
BTR:PCBM	12.7	75	0.90	8.6
	± 0.5	± 2.0	± 0.005	± 0.5
PM6:Y6	22.7	69	0.85	13.4
	± 0.5	± 2.0	± 0.005	± 0.5

SI Figure 3. (left) JV-curves of evaporated OSCs and solution processed reference OSCs used for the optoelectronic characterisation. The legend shows the active layer thickness. **(right)** JV-parameters of the OSCs. Additionally, the standard errors associated with the measured JV-parameters based on four pixels are shown for the VP-OSCs. The quoted standard errors for the SP-OSC references are based on an estimation of typical SP-OSC batches and are typically far greater than the variations observed in the VP-OSCs studied here-in.
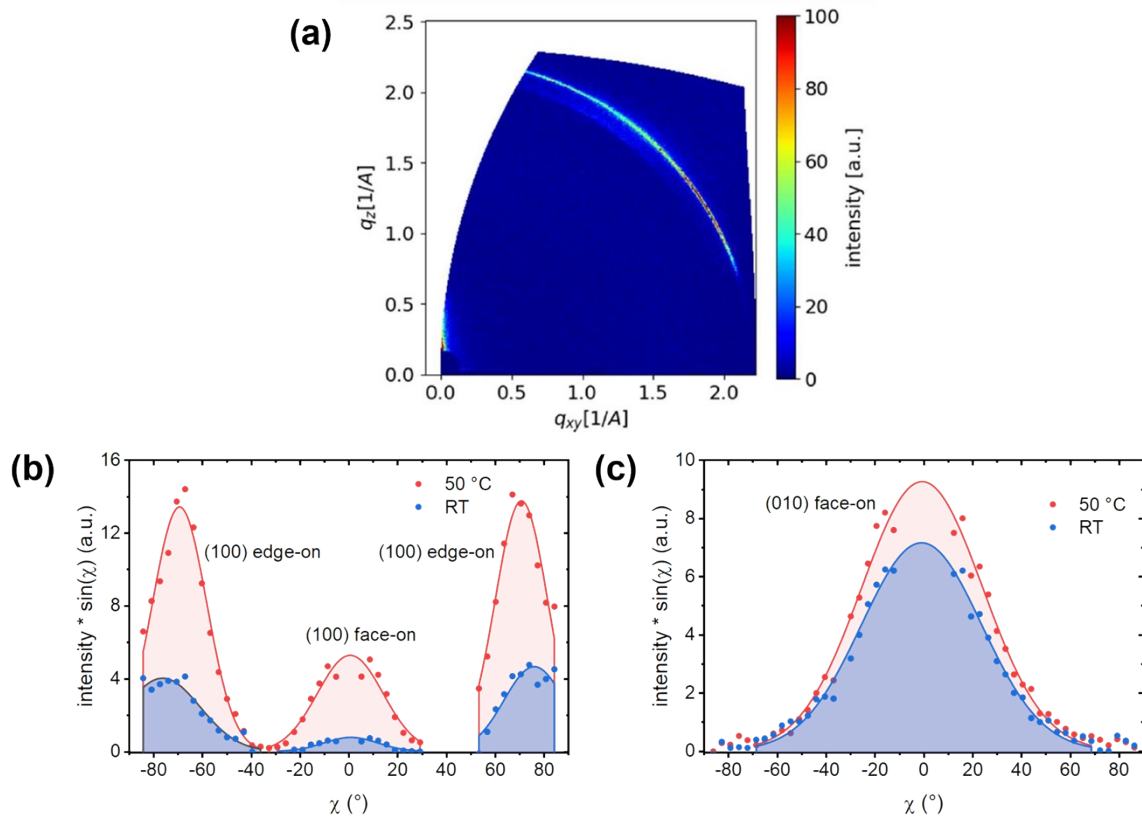
SI Figure 4. (a) 2D-GIWAXS diffraction pattern of the edged Si substrate showing a similar specular reflection as observed for the *RT* diffraction pattern shown in the main text. While the position is slightly changed due to a small incidence angle variation, this demonstrates that this feature arises from the Si substrate rather than the organic layers as would be expected for such a sharp feature. **(b), (c)** Pole figures obtained from azimuthal tube cuts of the (100) and (010) reflexes, respectively. The Gaussian fits are shown in solid lines.
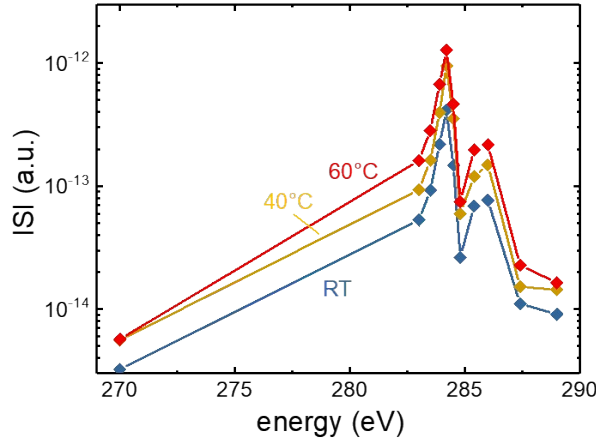
SI Figure 5. Energy-dependent ISI for BHJs deposited at different substrate temperatures. The stack is C_{60}/BHJ/BPAPF. The ISI spectrum follows characteristic material contrast functions of fullerene blends with maximum scattering observed at 284.2eV. We thus attribute the scattering feature at $q \sim 0.3\,nm^{-1}$ in **Figure 3 (d)** to domains with different compositions of DCV-V-Fu-Ind-Fu-V and C_{60}. While the shape of the ISI-energy spectra remains unchanged, the intensity increases for samples deposited at elevated temperatures, indicating increased domain purity, as discussed in the main part.
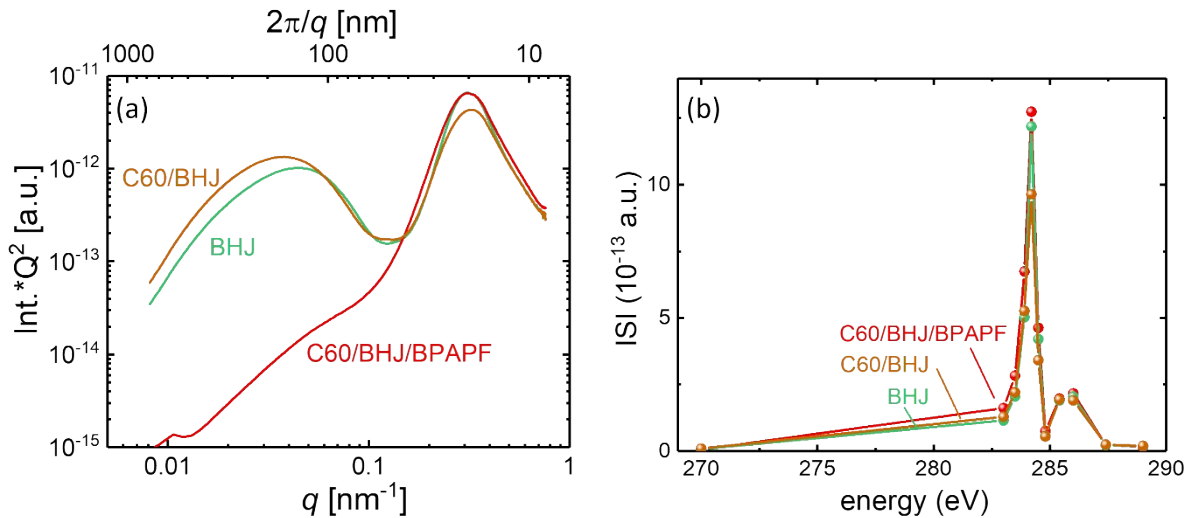

SI Figure 6. Influence of different layer stacks, with the BHJ deposited at 60°C, on the scattering signal. **(a)** Scattering profile at resonance (284.2eV), where scattering intensity is maximum. **(b)** Energy-dependence of the ISI. To obtain the same layer growth in the RSoXS samples compared to the devices, the DCV-V-Fu-Ind-Fu-V : C_{60} blends shown in **Figure 3 (d)** were deposited on an underlayer of C_{60}. Furthermore, the blends were capped with a BPAPF layer to prevent any potential surface reconstruction and lock in the film microstructure. Thereby, a blend microstructure that is representative of the device is ensured. Shown here is the influence of different stacks on the scattering profiles and ISI energy dependence. The main difference in **(a)** is in the low q region with a feature size of ~150 nm, which can be attributed to differences in scattering at the blend/vacuum and blend/BPAPF interface. Amorphous transport layers such as BPAPF are known to reduce surface roughness. Importantly, the low q region has little influence on the ISI, particularly at resonance, so that comparison of the ISI can be interpreted as changes in the domain composition – i.e. the relative domain purity - following Porod invariance analysis.

8
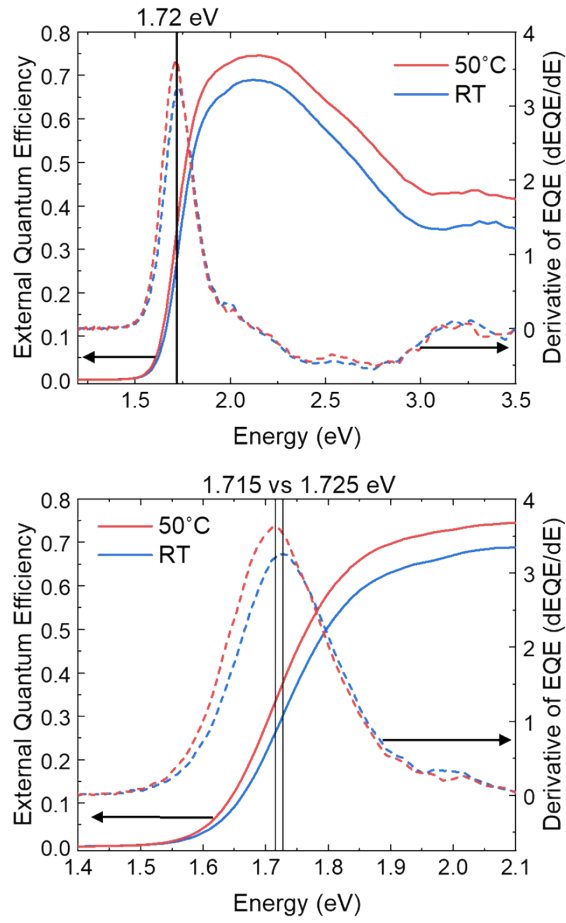
SI Figure 7. EQE and derivative of the EQE versus photon energy used to determine the effective photovoltaic gap according. Only a small redshift of about 10 meV is discernible for the *50℃* device.
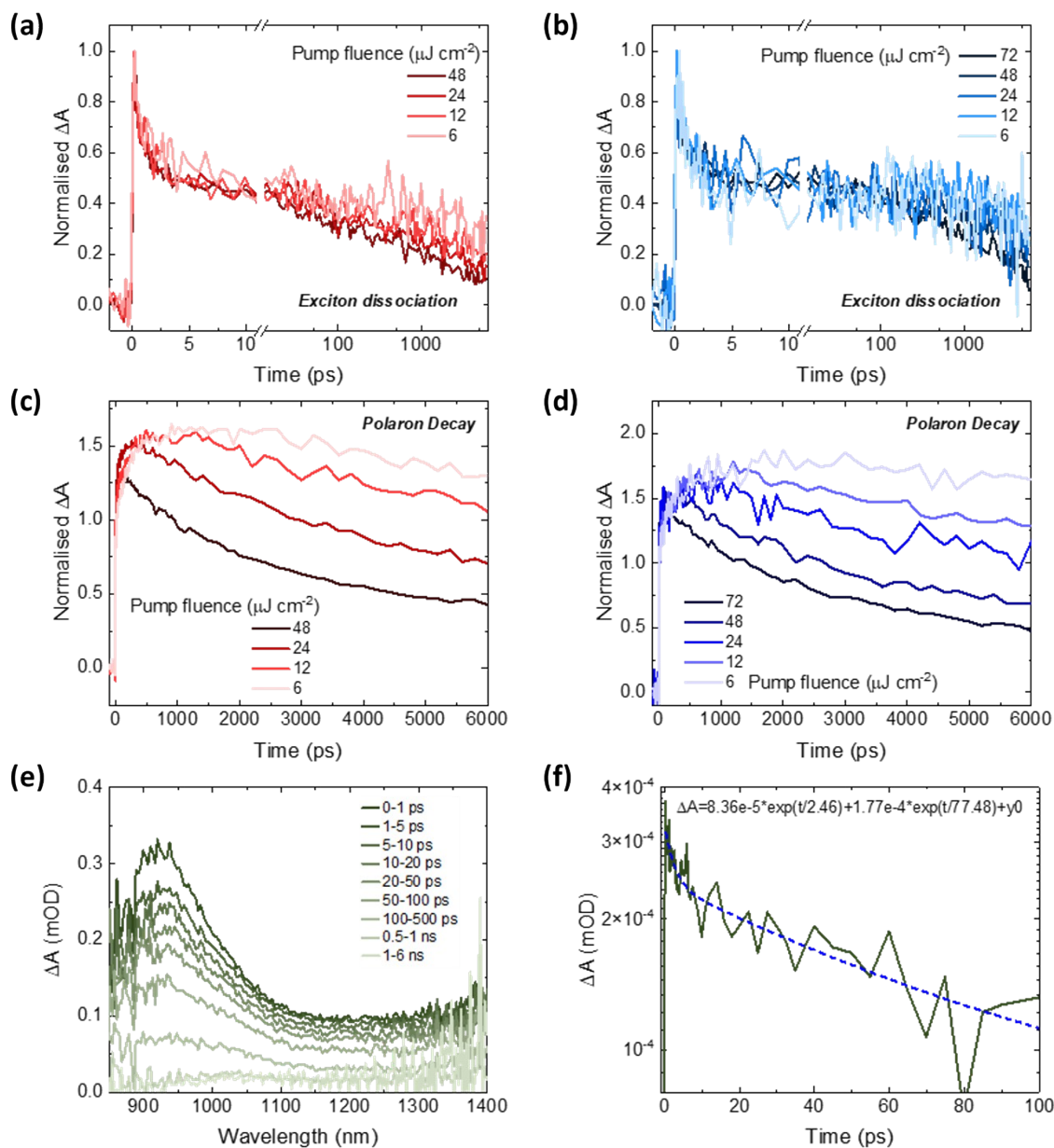
SI Figure 8. (a), (b) Fluence dependent decay of the exciton signal between 900 and 920 nm for the *50˚C* and *RT* film, respectively. **(c), (d)** Fluence dependent decay of the signal assigned to the hole polaron between 1050 and 1070 nm for the *50˚C* and *RT* film, respectively. Bimolecular fits to these spectra were used to calculate k_{BI} together with the charge carrier density estimated from the pump power and the film absorbance. **(e)** Ultrafast TAS spectra of the neat donor film recorded under identical conditions as the BHJ films. A pump fluence of 2 µJ cm^{-2} was chosen to minimize exciton-exciton annihilation effects. The amplitude weighted biexponential lifetimes were used to calculate an exciton lifetime of approximately 53 ps.
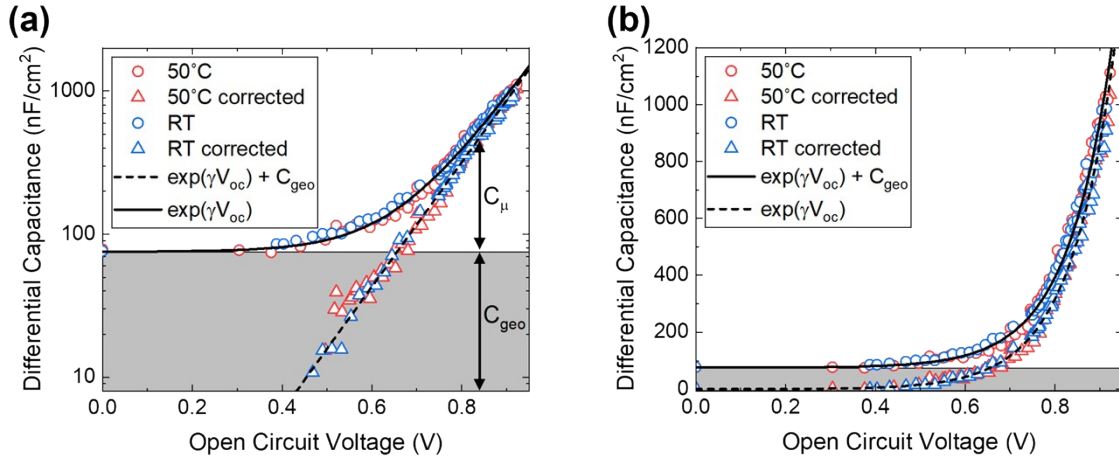
SI Figure 9. Differential Capacitance (DC) of the *RT* and *50°C* devices. The graphs show the total capacitance and the values corrected for the geometric capacitance together with the corresponding fits. The similar values of the geometric capacitance confirm the very similar active layer thickness of both devices.
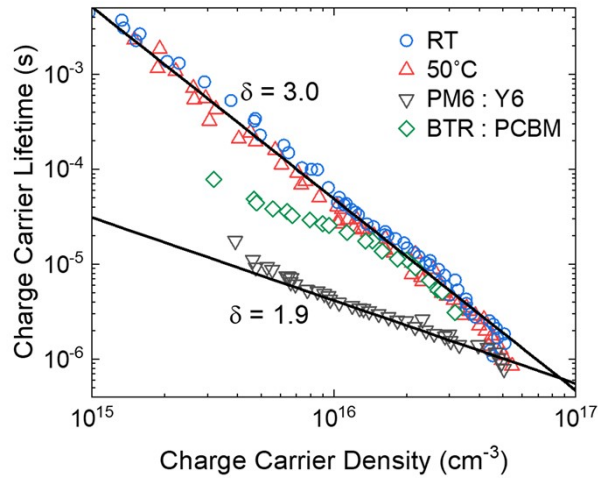

SI Figure 10. Charge carrier lifetime determined from TPV versus the spatially averaged charge carrier density determined from differential capacitance measurements. The recombination order calculated from the fits is provided.
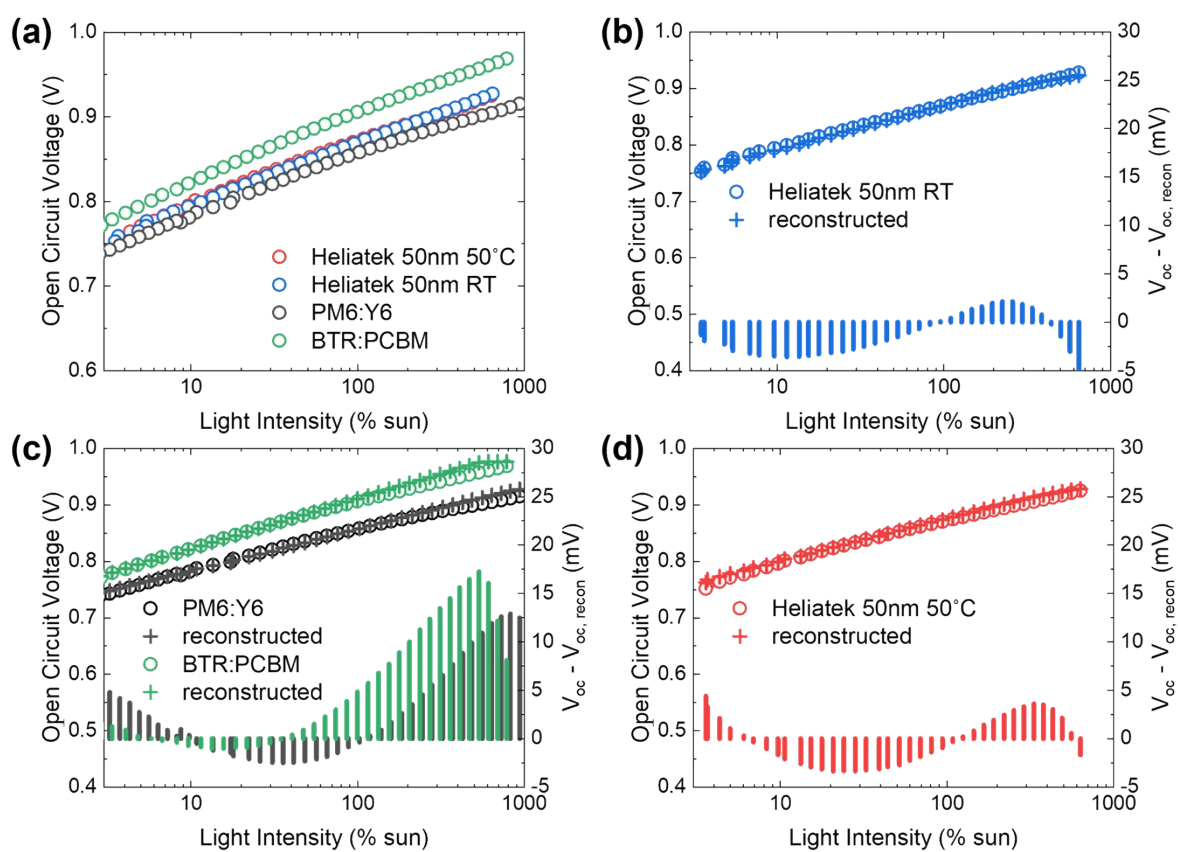
SI Figure 11. (a) Open circuit voltage as a function of light intensity. **(b), (c), (d)** Measured and reconstructed open circuit voltage of the respective devices. The right axis shows the residual of the reconstructed value subtracted from the measured value.
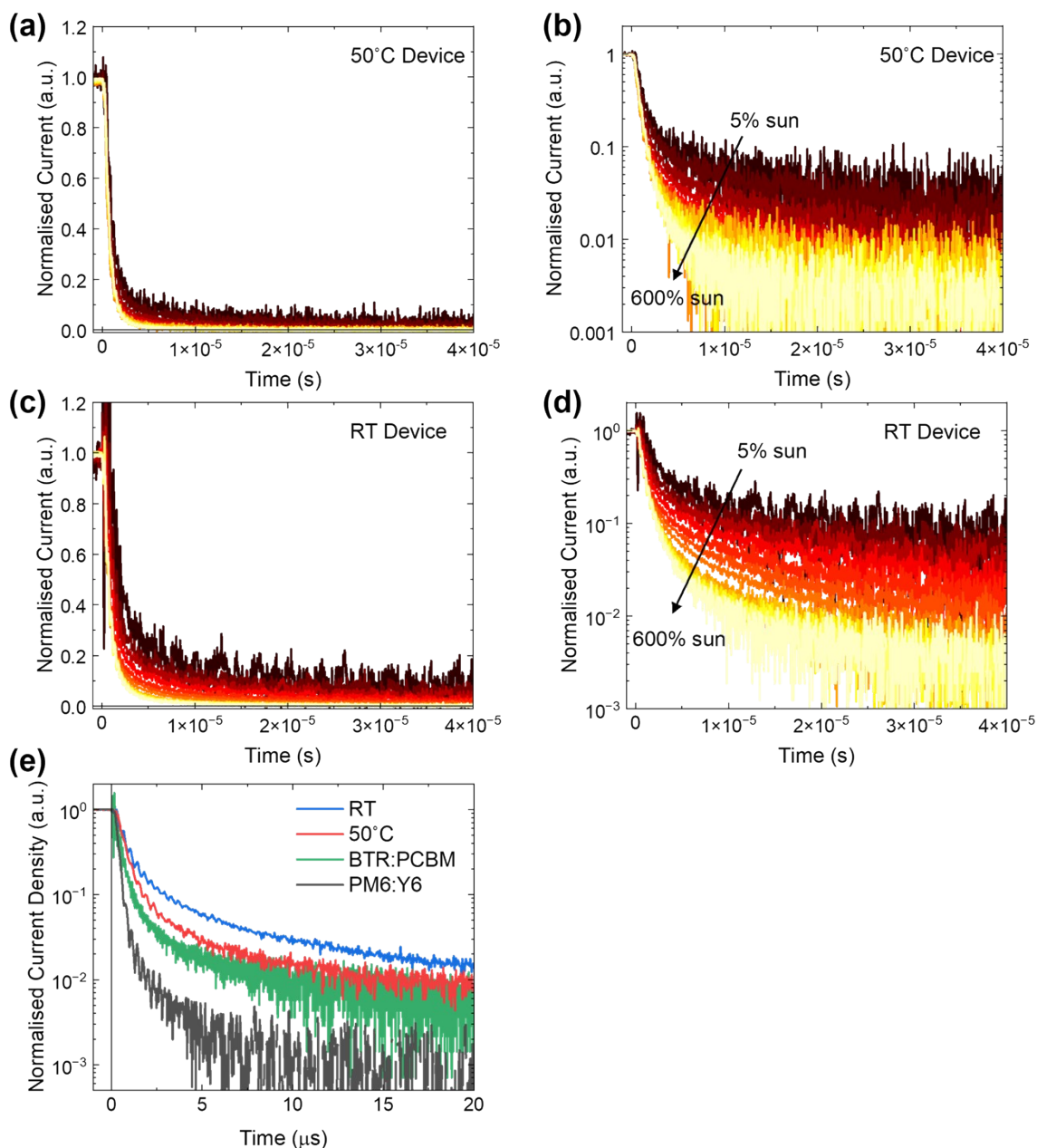
SI Figure 12. Charge extraction transients upon switching off the LED illumination at short circuit conditions that were used to characterise the effective mobility. Normalised transients recorded following different levels of LED illumination from 5% to 600% 1 sun equivalent illumination on a linear and logarithmic scale for the *50°C* (**(a)** and **(b)**, respectively) and *RT* device (**(c)** and **(d)**, respectively). **(e)** shows the charge extraction transients at 1 sun equivalent LED illumination for the *RT* and *50°C* device as well as BTR:PCBM and PM6:Y6.
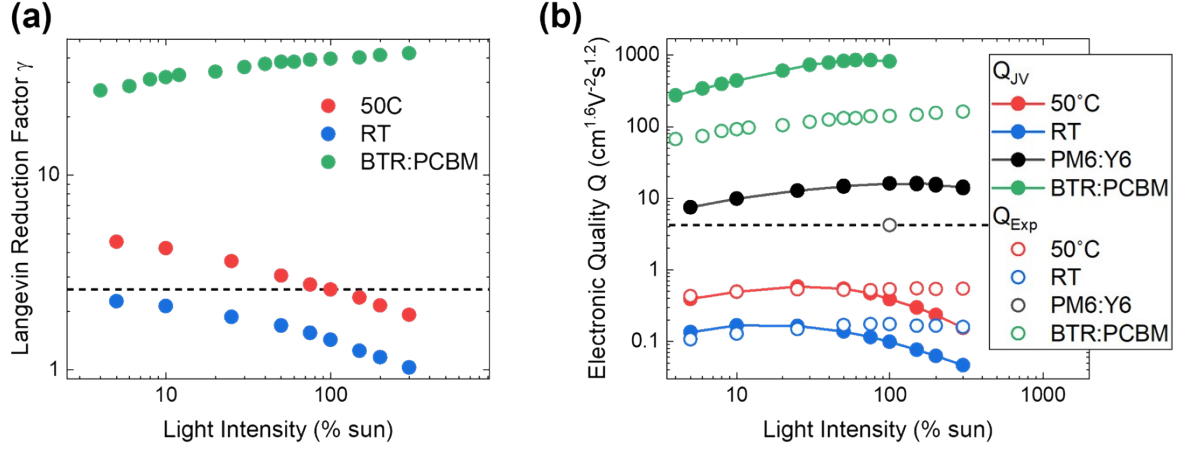
SI Figure 13. (a), (b) Light intensity dependence of the Langevin reduction factor and electronic quality, respectively. The electronic quality Q was determined from JV-curves (Q_{JV}) and optoelectronic measurements (Q_{Exp}). The results demonstrate that quoting a single value for the Langevin reduction factor without reference of the charge carrier density may be less comparable across different devices. The discrepancies between the values of Q determined by the different methods may have a variety of reasons such as the oversimplification of equating the generation current and J_{SC}, especially at high light intensity. To calculate Q_{Exp} the charge carrier density at MPP was estimated by assuming the difference of J_{SC} and J_{MPP} to be a reasonable measure for the bimolecular loss current. By applying the recombination kinetics determined from TPV and DC measurements, an estimate of the charge carrier density corresponding to the loss current is possible when assuming a simple zero-dimensional model. μ_{eff} and k_{BI} are taken at this value of n_{MPP} to calculate γ and Q_{Exp}.

SI Table 1. Simulation parameters used for the OghmaNano simulations. The parameters for the *RT* and *50˚C* device were obtained by a global fit to the experimental data as shown in **SI Figure 14** and **SI Figure 15**. The last column shows hypothetical parameters to achieve 9.4 % PCE and 10 % PCE for an active layer thickness of 50 nm and 70 nm, respectively. The changed parameters are highlighted in bold.

| Parameter	Units	*RT*	*50˚C*	*50˚C* $+ E_{ch} + n_{trap} + \mu_{free}$
Electron Trap Density	m^{-3} eV^{-1}	1.11×10^{23}	4.14×10^{24}	**2×10^{24}**
Hole Trap Density	m^{-3} eV^{-1}	7.87×10^{24}	4.00×10^{24}	**2×10^{24}**
Electron Tail Slope	eV	0.120	0.089	**0.05**
Hole Tail Slope	eV	0.120	0.089	**0.05**
Free Electron Mobility	m^2 V^{-1} s^{-1}	8.43×10^{-9}	1.17×10^{-8}	**2.17×10^{8}**
Free Hole Mobility	m^2 V^{-1} s^{-1}	8.43×10^{-9}	1.17×10^{-8}	**2.17×10^{8}**
Free Electron to Trapped Electron	m^{-2}	2.54×10^{-22}	8.21×10^{-22}	8.21×10^{-22}
Trapped Electron to Free Hole	m^{-2}	5.32×10^{-23}	1.04×10^{-22}	1.04×10^{-22}
Trapped Hole to Free Electron	m^{-2}	5.32×10^{-23}	1.04×10^{-22}	1.04×10^{-22}
Free Hole to Trapped Hole	m^{-2}	2.54×10^{-22}	8.21×10^{-22}	8.21×10^{-22}
Effective Gap	eV	1.3	1.3	1.3
Photon Efficiency	%	88.1	96.4	96.4
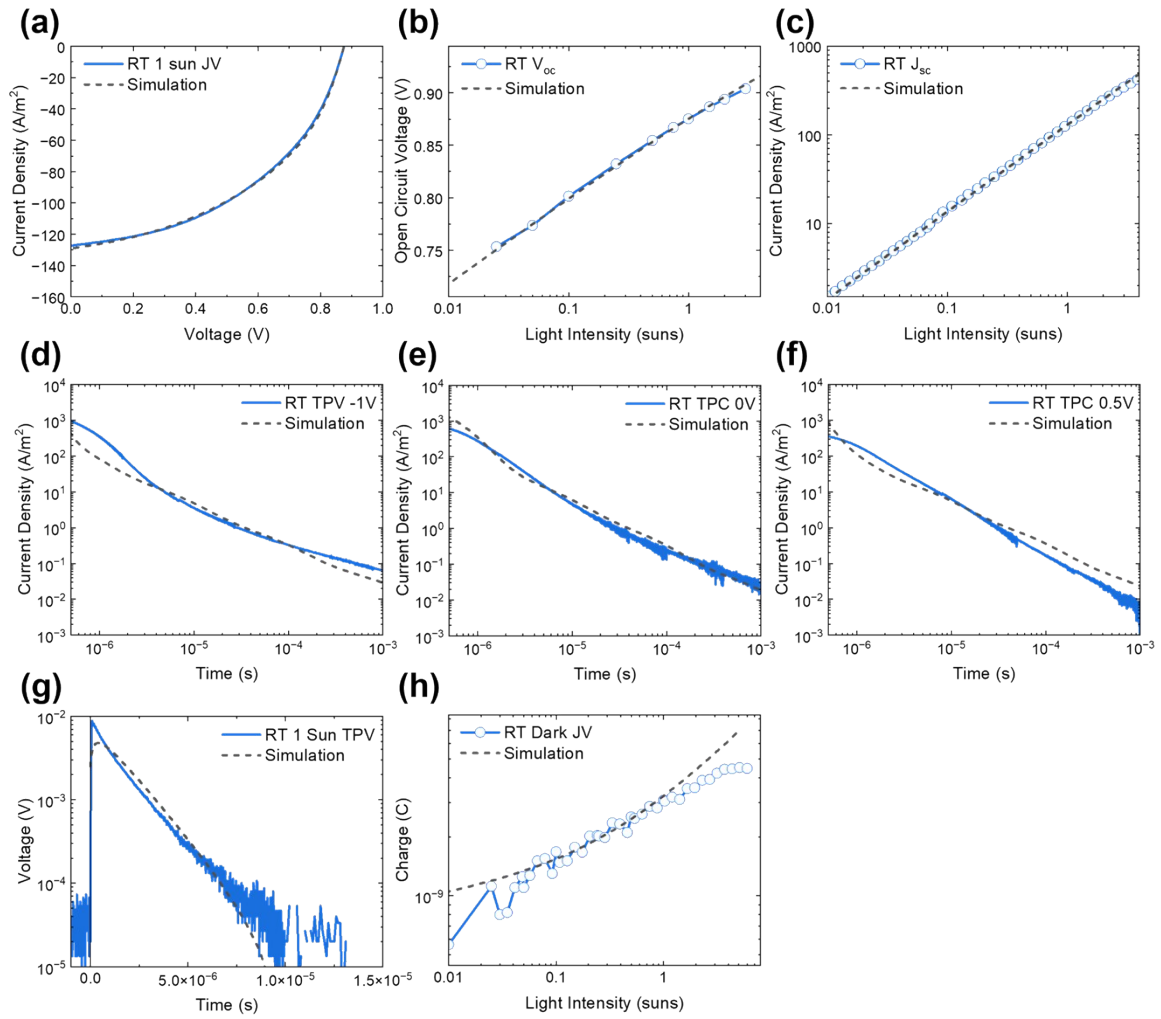
SI Figure 14. Global fit of experimental data using simulation software OghmaNano for the *RT* device. **(a)** 1 sun *JV*-curve. **(b)** V_{OC} vs. light intensity. **(c)** J_{SC} vs. light intensity. **(d), (e), (f)** Photocurrent transients recorded at -1V, 0V and 0.5V, respectively. Photocurrent transients were recorded as outlined by Street.[8] **(g)** 1 sun TPV transient. **(h)** Charge vs. light intensity.
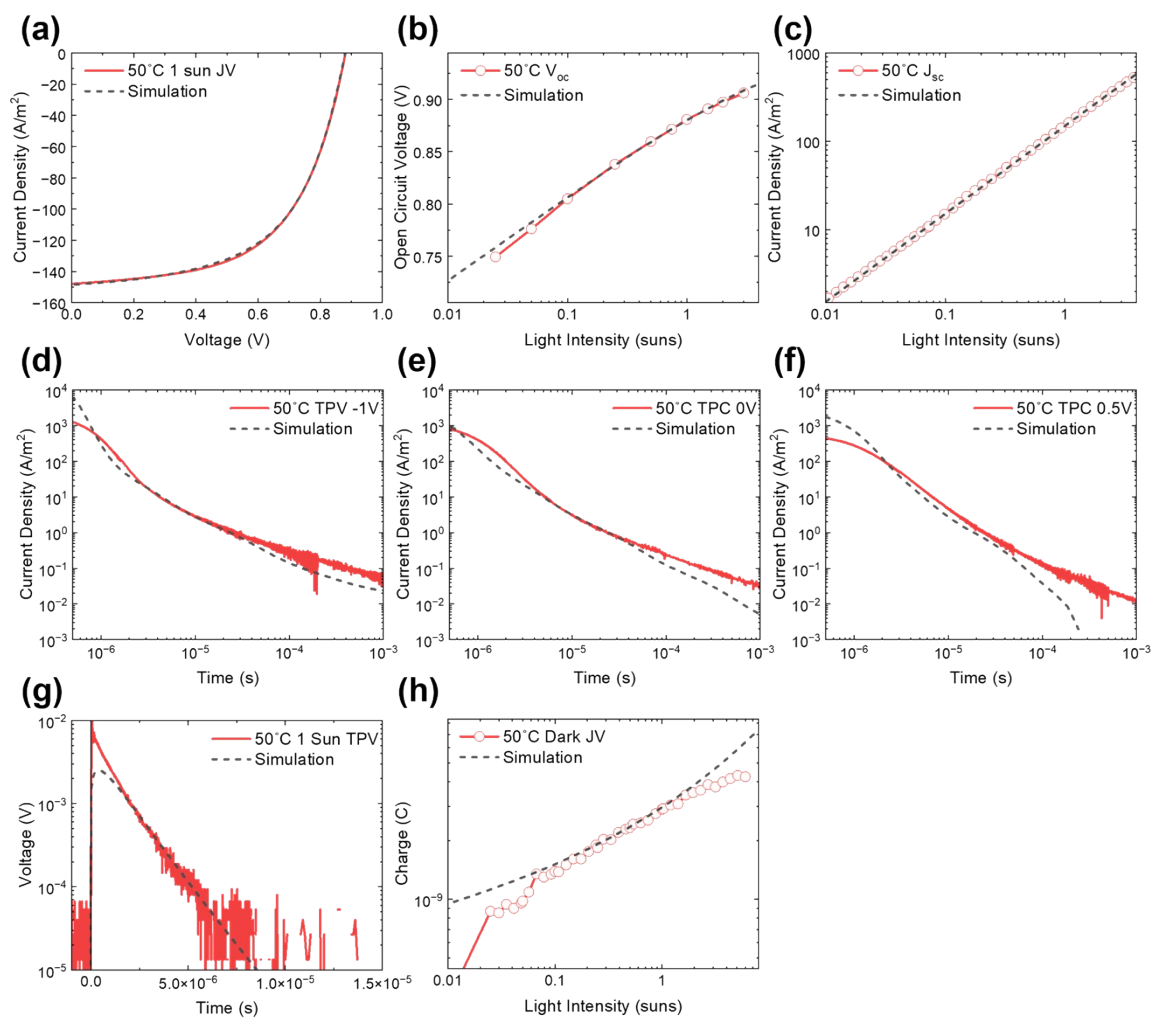
SI Figure 15. Global fit of experimental data using simulation software OghmaNano for the *50˚C* device. **(a)** 1 sun *JV*-curve. **(b)** V_{OC} vs. light intensity. **(c)** J_{SC} vs. light intensity. **(d), (e), (f)** Photocurrent transients recorded at -1V, 0V and 0.5V, respectively. Photocurrent transients were recorded as outlined by Street.[8] **(g)** 1 sun TPV transient. **(h)** Charge vs. light intensity.
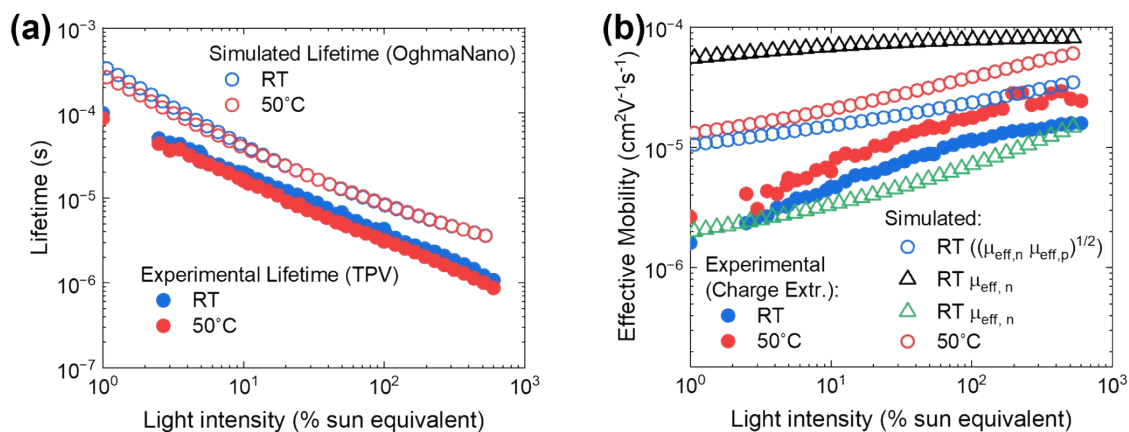
SI Figure 16. Comparison of experimental data with simulated data obtained from global fit parameters shown in SI Table 1 for the *RT* and *50°C* device. **(a)** Experimental obtained from TPV and simulated spatially averaged charge carrier lifetime. **(b)** Experimental effective mobility obtained from charge extraction measurements and simulated effective mobility. Note that in the case of *50°C*, the tailslopes and free mobility values for holes and electrons were assumed to be near identical leading to identical effective mobilities at different levels of trap filling. For *RT* the tailslopes were not identical and therefore the effective electron and hole mobility are shown as well as their geometric mean. The geometric mean was chosen following work by Heiber *et al.*[9]
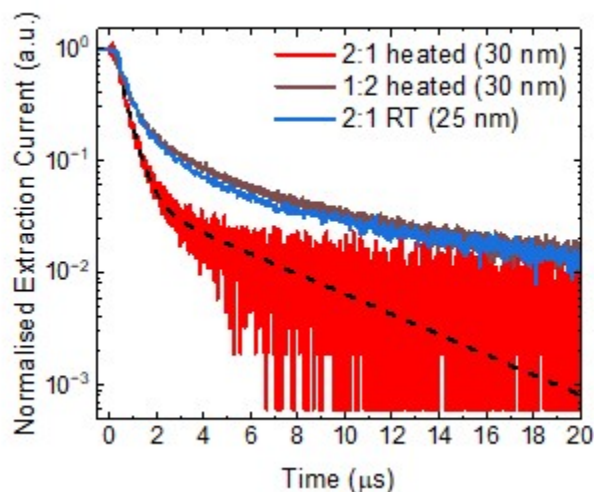
SI Figure 17. Normalised photocurrent transients recorded following switching off the 1 sun illumination LED illumination. The device devices are kept at short circuit throughout. The devices shown here were deposited at different substrate temperatures and with varying D/A ratio. While the active layer thickness varied slightly (see brackets in legend), the results illustrate that lowering the donor content results in a similar increase of the slow extraction transient as depositing the active layer at room temperature that resulted in an increase in the amorphous donor phase.
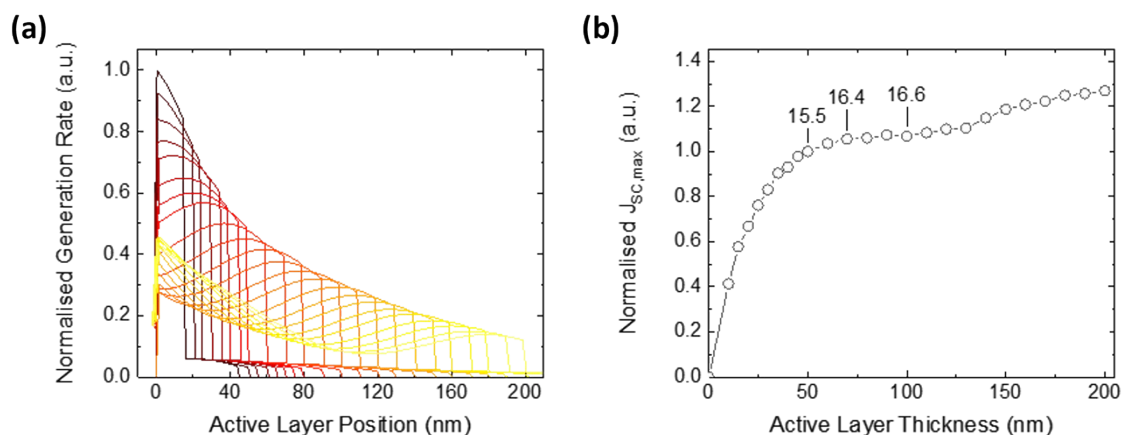
SI Figure 18. (a) Absorption profile calculated using transfer-matrix simulations built-in to OghmaNano with n, k data obtained by Heliatek GmbH. Note that the interlayer configuration was not changed and the thickness of doped transport layers that can act as optical spacers was not optimised. **(b)** Maximum achievable generation current as calculated from the integrated absorption profiles.

References

1   E. Gann, A. T. Young, B. A. Collins, H. Yan, J. Nasiatka, H. A. Padmore, H. Ade, A. Hexemer and C. Wang, Soft x-ray scattering facility at the Advanced Light Source with real-time data processing and analysis, Review of Scientific Instruments, 2012, 83, 045110.

2   J. Ilavsky, Nika: software for two-dimensional data reduction, J Appl Cryst, 2012, 45, 324–328.

3   S. Mukherjee, C. M. Proctor, G. C. Bazan, T.-Q. Nguyen and H. Ade, Significance of Average Domain Purity and Mixed Domains on the Photovoltaic Performance of High-Efficiency Solution-Processed Small-Molecule BHJ Solar Cells, Advanced Energy Materials, 2015, 5, 1500877.

4   C. G. Shuttle, B. O'Regan, A. M. Ballantyne, J. Nelson, D. D. C. Bradley and J. R. Durrant, Bimolecular recombination losses in polythiophene: Fullerene solar cells, Phys. Rev. B, 2008, 78, 113201.

5   C. G. Shuttle, R. Hamilton, J. Nelson, B. C. O'Regan and J. R. Durrant, Measurement of Charge-Density Dependence of Carrier Mobility in an Organic Semiconductor Blend, Advanced Functional Materials, 2010, 20, 698–702.

6   C. G. Shuttle, B. O'Regan, A. M. Ballantyne, J. Nelson, D. D. C. Bradley, J. de Mello and J. R. Durrant, Experimental determination of the rate law for charge carrier decay in a polythiophene: Fullerene solar cell, Appl. Phys. Lett., 2008, 92, 093311.

7   D. Credgington, S.-W. Liu, J. Nelson and J. R. Durrant, In Situ Measurement of Energy Level Shifts and Recombination Rates in Subphthalocyanine/C 60 Bilayer Solar Cells, The Journal of Physical Chemistry C, 2014, 118, 22858–22864.

8   R. A. Street, Localized state distribution and its effect on recombination in organic solar cells, Phys. Rev. B, 2011, 84, 075208.

9   M. C. Heiber, C. Baumbach, V. Dyakonov and C. Deibel, Encounter-Limited Charge-Carrier Recombination in Phase-Separated Organic Semiconductor Blends, Phys. Rev. Lett., 2015, 114, 136602.